

Characterization of a Superconducting nanowire single photon detector

Max Reicherd

Bachelorarbeit in Physik
angefertigt im Institut für Angewandte Physik

vorgelegt der
Mathematisch-Naturwissenschaftlichen Fakultät
der
Rheinischen Friedrich-Wilhelms-Universität
Bonn

Juli 2024

I hereby declare that this thesis was formulated by myself and that no sources or tools other than those cited were used.

Bonn,
Date
Signature

1. Reviewer: Prof. Dr. Sebastian Hofferberth
2. Reviewer: Prof. Dr. Daqing Wang

Acknowledgements

I would like to thank ...

You should probably use \chapter* for acknowledgements at the beginning of a thesis and \chapter for the end.

Contents

1	Introduction	1
2	Working principle of SNSPDs	2
3	Faint laser source for detector characterization	5
3.1	Characteristics of faint laser sources	5
3.2	Experimental setup	6
4	Characterization of a SNSPD by Single Quantum	9
4.1	Dark Count Rate	9
4.2	Recovery time	11
4.3	Efficiency	15
4.4	Discussion	21
5	Conclusion and Outlook	24
A	Appendix	25
A.1	ND filter calibration	25
A.2	Angle dependent countrate and η_{sde}	29
A.3	Recovery time measurements	29
A.3.1	Recovery time measurements - Oscillating bias current	29
A.3.2	Polarization alignment for system detection efficiency measurements	29
A.4	Recordings of analog pulses	29
A.5	Bias sweeping for different count rates	29

CHAPTER 1

Introduction

Single photon detection is an essential part in nonlinear quantum optics with Rydberg atoms. Nonlinear quantum optics with Rydberg atoms is used for the study of fundamental light matter interactions in the HQO (Hybrid Quantum Optics) experiment at the University of Bonn and might result in innovations for promising applications like optical quantum computing [[firstenberg-2016](#), [gao-2011](#)].

In the HQO experiment properties of Rydberg atoms will be used to interact with an electromechanical acoustic oscillator [[<empty citation>](#)]. For this study of those interactions, it is required to place the Rydberg atoms with the electromechanical acoustic oscillator in a 4K environment inside a cryostat (science chamber). Inside the science chamber Rydberg atoms will be trapped over atom chip. The goal is to excite Rydberg atoms and cool down the electromechanical acoustic oscillator to its ground state through the interaction with the Rydberg atoms.

The challenge of detecting single photons is to translate the low energies (input variable - e.g. for the optical/infrared range: $E \approx 0.5 - 3.3\text{eV}$) into measurable electrical signals (output variable). Four central requirements have been established in the literature to quantitatively describe the quality of EPD [8, 10].

CHAPTER 2

Working principle of SNSPDs

This chapter will introduce the working principle of superconducting nanowire single photon detectors (SNSPDs). It provides the principles in terms of their phenomenological aspects. For further details regarding the physics and mathematics behind superconducting nanowires, the reader is directed to the work of Gol'tsman et al [1] and Hadfield et al [2].

The SNSPD has four parts, as shown in figure 2.1. The central detection area is made of a superconducting nanowire ($\approx 100\text{nm}$ wide) on a sapphire base. To collect the whole output of the optical fibre, a pattern out of a thin superconducting film (like niobium nitride) is shaped into a meandering nanowire through nanofabrication [3]. The sapphire layer is used to dissipate the heat when the wire heats up. Further, a gold contact supplies a bias current through the superconducting nanowire and an optical fibre is coupled to the detection area.

To operate the system, the setup is cooled below the critical temperature of the superconductor to 2-3K and a DC current is applied to the nanowire.

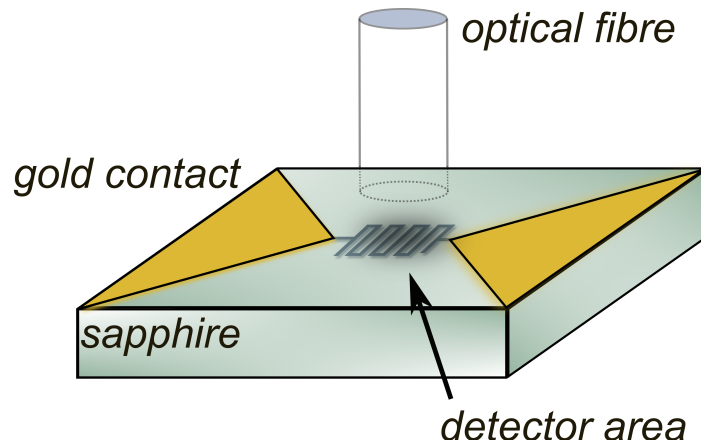


Figure 2.1: (a) Scematic illustration of the fundamental parts of a superconducting nanowire single photon detector [4]. Detector area is made of a superconducting nanowire and is contacted from two sides with gold. Optical fibre coupled to the detection area. The fibre coupling realization of the characterized detector from Single Quantum is shown in figure 2.4.

The detection process is shown in the figure 2.2.

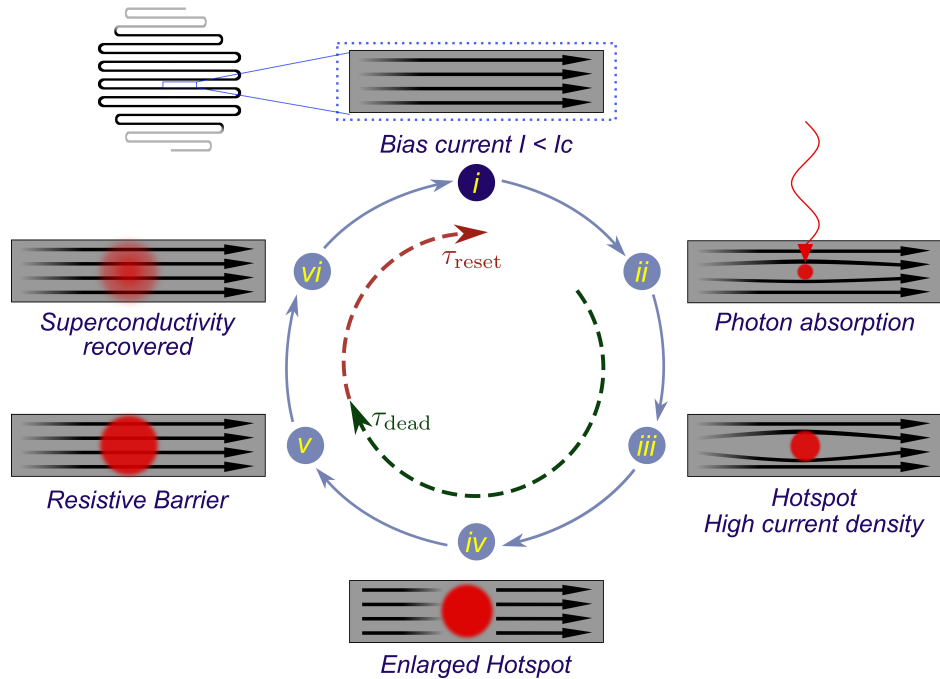


Figure 2.2: Schematic detection process cycle of a superconducting nanowire single photon detector [5]. Innercircle shows the parts of the dead time τ_{dead} and the reset time τ_{reset}

. Outer circle shows the parts of the detection process. In the upper left side, the whole detector area is shown, the rey bars show the current flow in the zoomed in superconducting nanowire.

Photons hit the superconducting nanowire (ii) and break up individual Cooper pairs. This leads to a local reduction of the critical current below the bias current and in turn to a localised area where the superconductivity is interrupted, this local area forms the so-called "hotspot" (iii). This hotspot forms a resistance area because the critical temperature is exceeded by the energy of the photon. In response, the current flows around this hotspot (iv), whereby the local current density in the side areas next to the hotspot again exceeds the critical current, due to a higher current density. If the critical current is exceeded, the superconductivity also breaks down in these areas. This excess also causes a resistance in the side channels of the nanowire (v). Ultimately, this rapid increase in resistance can be measured in form of a voltage pulse, which can be seen in figure 2.3. The local non-superconducting area is then cooled down by the cryogenic environment and returns to the superconducting state (iv—i).

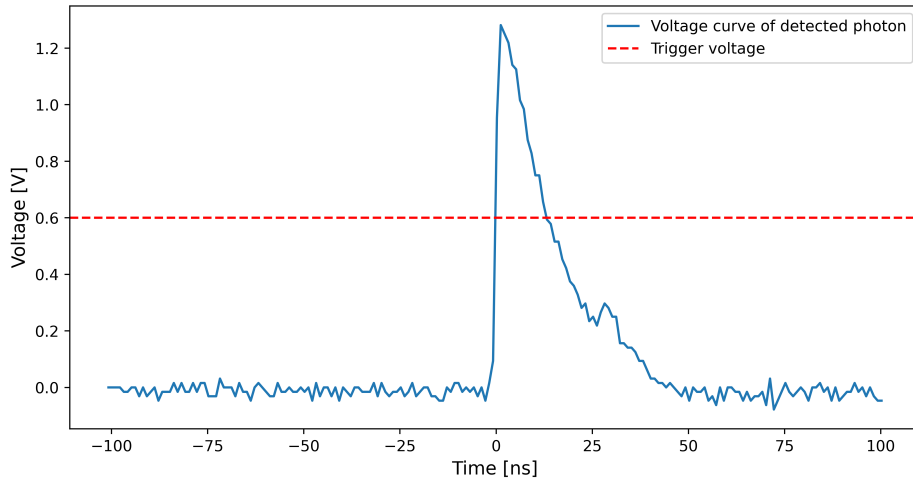


Figure 2.3: Single analog voltage pulse signal recorded with an oscilloscope from Lecrois with time resolution of 500MHz. Voltage is depicted on the Y-axis and time on the X-axis. Single photon stems from a faint laser source (780nm) attenuated to 1.6KHz.

Due to a polarization dependent absorption efficiency it is important to consider the technical detail of the geometry of the meander. In the used SNSPD, the meander design allows for a higher absorption efficiency if the e-field of the photons is parallel polarized to the wire direction than orthogonally polarized ones [3]. As depicted in figure 2.4 the coupled fibre slow axis in the characterized detector is parallel aligned to the nanowire to maximize the absorption efficiency. Other geometries are investigated and might enable a high absorption efficiency independent of the polarization [6].

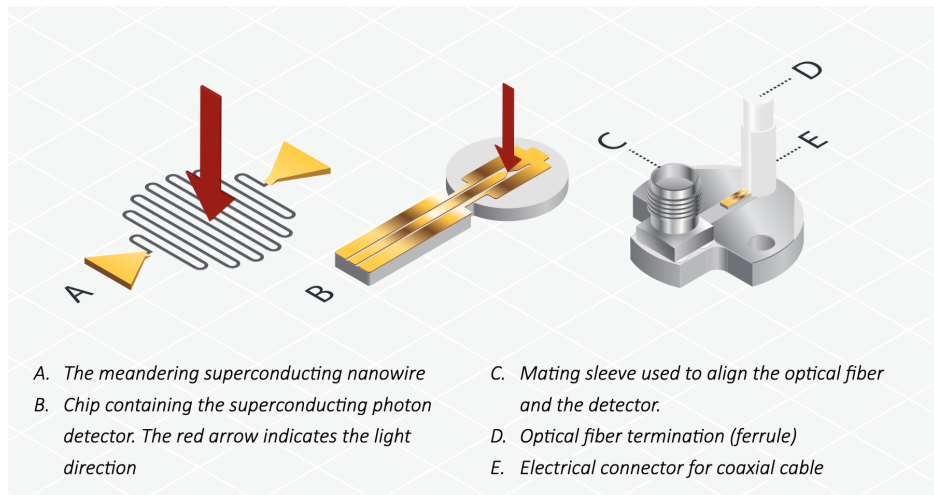


Figure 2.4: Fibre coupling set up to the superconducting nanowire detector area of the characterized detector by the Single Quantum [7]. Fibre coupling is made inhouse and is adjusted to maximize efficiency. Can can not be adjusted manually.

CHAPTER 3

Faint laser source for detector characterization

In order to characterize a detector, it is necessary to consider not only the characteristics of the detector itself, but also those of the emitter source. This section will focus on the characteristics of the laser setup, which serves as a light source for the detector characterization. In order to provide a brief overview of the characteristics of a coherent laser light source and the conditions it gives for detector characterization, I will first present a summary of the relevant information. Furthermore, I will introduce the setup that I have constructed for characterizing the SNSPD.

3.1 Characteristics of faint laser sources

Using a laser source enables us considering the emitting light as monochromatic beam with angular frequency ω and constant Intensity I . The Photon flux of a laser is defined as the photon average number passing through a cross-section in one unit time:

$$\Phi = \frac{IA}{\hbar\omega} = \frac{P}{\hbar\omega} \text{photons } s^{-1} \quad (3.1)$$

where I is the current of photon, A the cross-section, P the laser power and $\omega = \frac{2\pi c}{\lambda}$ the angular frequency which depends on the wavelength. The average number of registered counts $N(T)$ for a given detection time T by a detector is given by:

$$N(T) = T\Phi\eta = \frac{P T \eta}{\hbar\omega} \text{photons} \quad (3.2)$$

and hence the registered counts \mathcal{R} per unit time is described by:

$$\mathcal{R} = \frac{N(T)}{T} = \eta\Phi = \frac{P\eta}{\hbar\omega} \text{photons } s^{-1} \quad (3.3)$$

where η is the efficiency of the detector system which is described in more detail in section 4.3.

The detector has a maximal detection count rate, and it is restricted by the recovery time ($\tau_{\text{recovery}} = \tau_{\text{rec}}$)[4.2](#) of the detector $\mathcal{R}_{\max} \propto \frac{1}{\tau_{\text{rec}}}$.

Sending too many photons at once to the detector causes latching and prevents counting [3]. Therefore, the photon rate send to the detector has to be below the maximal detection count rate of the detector. As consequence for this experiment, the laser power has to be attenuated to a level where the photon rate is below the maximal detection count rate of the detector.

The photon statistic of coherent light, in our case (in reasonable approximation) of our laser light, is given by poisson statistics.

This property originates from the discrete nature of photons, which are randomly distributed with non-equidistant spacing between each other.

Considering the fact, that the detector is not able to detect photons within the deadtime and with significant lower efficiency in the reset time, one has to look at the probability of photons in those blind spots to include this in later efficiency evaluation.

The amount of photons is calculated by looking at the probability measuring one photon per length segment, given by the deadtime and the reset time. First, we consider one Length segment given by the deadtime τ_d :

$$L_d = c \cdot \tau_d \quad (3.4)$$

$$(3.5)$$

c denotes the speed of Light. With this, we can calculate for a given measurement time the average photon rate \bar{n} per length segment L_d

$$\bar{n} = \Phi \frac{L_d}{L_c} \quad (3.6)$$

$$(3.7)$$

L_c denotes the length of light passing in one second. This enables us to calculate the probability, given by the poisson distribution,

$$P_{\text{dead}}(n) = \frac{(\bar{n})^n}{n!} e^{-\bar{n}} \quad (3.8)$$

of finding n Photons within the length segment, defined by the dead time τ_d .

In accordance with the specified probability, the quantity of photons that are inherently unmeasurable due to the constraints of the detector can be calculated.

3.2 Experimental setup

From factory details it is known that the recovery time of the detector is located between 17 and 23ns, depending on the detector settings. This details can be confirmed by our measurements as well [4.2](#). This gives a theoretical maximum detection rate with constant maximal possible efficiency of $\mathcal{R}_{\max} \propto \frac{1}{\tau_d} \approx 43 - 58\text{MHz}$. However, this rate would only hold, if the emitter would be a true single

photon source with a consistent emitting rate, where photons are equidistantly spaced. Since we use a coherent laser source the counting rate is significantly lower than the theoretical maximum detection rate. From the factory we got specification of about 2-4 MHz as detection count rate with maximal detection efficiency **Source**.

The initial situation is that the minimum laser power of the laser source is higher than the maximal detection count rate of the detector. The reason for this is that the laser source does only lase with a constant power with a certain minimum power. Therefore, the laser power can not be regulated down by adjusting the input power of the laser, but has to be attenuated by neutral density filters afterwards.

In order to realize the laser attenuation the setup shown in fig 3.1 was build. The first coupling of the laser light at the upper stage was done in order to operate with the beam on the lower stage, because the laserbeam was due to its construction on an uplifted stage. Afterwards, on the lower stage the beam passes a half-wave plate λ_2 and polarization beam splitter (pbs) to filter the horizontal polarized E-field out. Further, a galilei telescope was build (l_1 and l_2) out of one focal and one diffusing lens for reducing the beam width, so it fits fully on the surface of the crystal of the Acousto-optic modulator (AOM). The first order of the AOM was used for flexible voltage modulation of the laser. A cover was used to filter out the first from the zeroth order of the AOM. Then a flip mount was placed, where Neutral density (ND) filers could be placed in and flexible placed in and out of the laser beam. The ND filters have the function to attenuate the laser light. At the end, before the laser light was again coupled in, again a half-wave plate λ_2 and quarter-wave plate λ_4 were used to stabilize and control the light polarization coupling in the fibre. As mentioned in 2 the light was polarized according to the slow axis of the fibre. Afterwards the light was coupled back into a fibre, so it was directed to the detector. Technically, it was important coupling to a APC/PC to FC/PC optical fibre because the detector only had an FC/PC optical fibre input port, in order to maintain higher efficiency coupling in the light [3].

Besides, this optical setup had to be protected from environmental light. For this, the room where the setup was running was shielded with alu foil which has a reflection coefficient of almost 90% at the operating wavelength of 780nm **Source**. Moreover, a black box was build. It has the function to avoid further environmental light coupling into the fibre. Additionally, the optical fibre running from the optical setup to the detector was shielded with alu foil as well to avoid absorption from the optical fibre.

Based on those theoretical considerations and our experimental setup, one can approach the central goal to determine the amount of photons and with this, determine the efficiency of the detector.

Central, in order to do efficiency measurements, on the one hand one must send only a few photons (low power) and one must exactly know how many photons are send. For this we need to measure the power of the laser light, we are sending to the detector. However, the desired light is so weak, we cannot measure it with power-meters or any other measurement devices available to us. So our photon rate we are expecting to send to the detector depends on the ND filters and their optical density (OD) value, since it is the sole factor we can adjust our laser power (here transmission)($T = 10^{-OD}$), hence our amount of photons we send to the detector.

The challenge relying on ND filters is that the fabric values of their OD are not precise, hence the filters need to be calibrated by oneself and as precise as possible, to get accurate and stable OD values for the ND filters.

To get accurate results, the OD value of each filter is measured with two methods to reduce

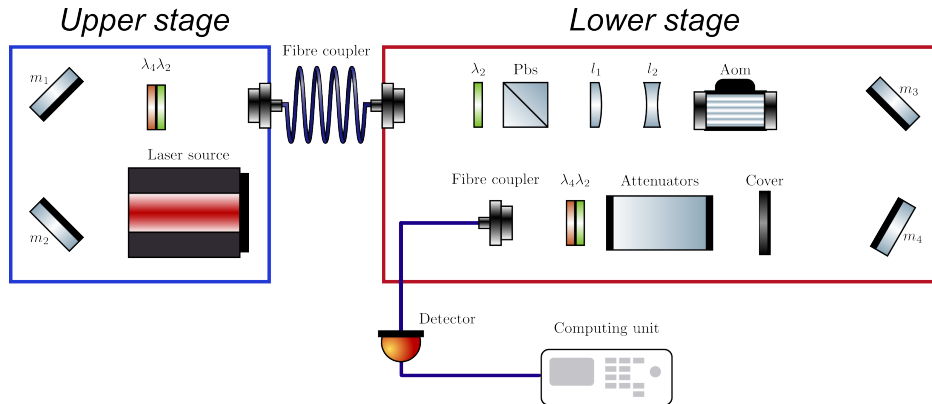


Figure 3.1: Set up for attenuation of a 780nm laser source from the Russian company [Vitawave](#)

systematic errors. The first method measures the OD values, where the ND filters are set in the flip mount as shown in graph 3.1. The second method measures the OD values after the fibre coupling directly in front of the powermeter outside the blackbox to avoid straying light from the elements in the setup.

The attenuation of ND filters is quantized via the OD value and is connected to the transmission value $T = 10^{OD}$ of the outgoing light. Due to the logarithmic definition of the OD value, the OD values of the ND filters are added up when they are stacked on each other.

The measurement of the OD values was done by sending light on the filter and measuring the power with and without the filter. Moreover, only single ND filter measurements were in the measurable range, since the powermeter was not able to measure the power of the attenuated laser light by several stacked ND filters.

The OD value is then calculated by the logarithmic value of the inverse transmission value $\log_{10}(\frac{1}{T})$. The transmission value is given by the proportion of the power with the filter compared without the filter $T = \frac{P_{out}}{P_{in}}$. Afterwards, the final OD values of each method were combined and the corresponding systematic and statistical errors are considered in order to get accurate OD values for the ND filters. Results of the measurements and error calculations can be found in section ??.

Based one these OD values the photon rate was determined.

CHAPTER 4

Characterization of a SNSPD by Single Quantum

In literature, four central characteristics have emerged to quantify the quality of single photon detectors and make their performance comparable [2, 8]. These characteristics are the system detection efficiency η_{sde} , the dark count rate (DCR), the recovery time ($\tau_{\text{recovery}} = \tau_{\text{rec}}$) and the timing jitter. In this thesis, I focus on the detector efficiency η_{sde} , the dark count rate (DCR) and the recovery time (τ_{rec}). In general there are more than these introduced figures of merits, like after-pulsing but these will not be considered in this thesis.

4.1 Dark Count Rate

The DCR is the rate of measured detection events not intentionally sent from the source (here the faint laser source). It is measured in counts per second and can be caused by statistical fluctuations in the measurement electronics. A low DCR is important for a high signal-to-noise ratio and means easy interpretable results which are not distorted by noise [9].

In the context of SNSPDs, the DCR is dependent on the bias current applied to the nanowire. This is due to the fact that if the bias current approaches the critical current, less current $\Delta I = I_c - I_B$ is needed to exceed the critical current. Therefore, electronic fluctuation, close to the critical current will cause a breakdown of the superconducting state and hence a dark count more often. Furthermore, it is important to perform DCR measurements first in the characterization process because it determines the limit, where general measurements are not distorted by high DCR noise.

Measurement and results

In order to evaluate the DCR, it is necessary to perform measurements in two different setups. First, a setup in which no optical fibre is connected to the detector and the port is covered. In such a setup, it can be assumed that no photons from the surrounding environment are striking the detector. This allows for the measurement of the DCR only triggered by the electronics noise depending on the detector's bias current and trigger voltage.

The required measurement setup consists out of the detector with the protection cap on the output port of the detector. This configuration represents the most shielded environment from external light sources and serves as the reference value for optimal DCR values achievable in single photon

measurements. The measurement was conducted by sweeping the bias current from 0 to $35\mu\text{A}$ in $0.1\mu\text{A}$ increments with an integration time of 200ms at each step

The second setup involves connecting the detector to the faint laser source of section 3.1. The laser source was turned off, so no photons from the source were sent to the detector. This is done in order determine the DCR for consecutive measurements and improve the light shielding of the setup and the optical fibre. This allows one to find the optimal shielding configuration for the highest signal-to-noise ratio. Once more, the bias current was swept from 0 to $35\mu\text{A}$ in $0.1\mu\text{A}$ increments with an integration time of the count rates for 200 ms. In fig 4.1 the results are shown for an optimized and a non optimized case.

At the initial, non optimized configuration an optical fibre was connected to the detector's output port and the fibre output coupling of the experiment. The laser source was turned off, so only electronic fluctuations and ambient light hitting the detector can cause detection events. To reduce dark counts due to ambient light a black box was constructed that covers the laser setup. Further, the fiber was wrapped in aluminum foil to prevent ambient light to couple to the core through the cladding.

As expected, the DCR rise in each case in 4.1 with decreasing difference $\Delta I = I_c - I_B$ due to raising probability that weak electronic noises trigger a signal. The orange curve in 4.1 demonstrates that in the absence of protection, a significant number of photons from the environment are able to enter the detector through various potential pathways like the fibre cladding or the coupling connection to the laser setup.

In contrast, the measurement results with full shielding, depicted in figure 4.1 as well, show, that the DCR of the coupled and protected setup is the same as to the DCR with a cap on. The peaks in the green curve at ≈ 3 and $\approx 14\mu\text{A}$ are artifacts resulting from some leakages in the protection. Nevertheless, these leakages are not substantial when viewed in the context of the total photon count rate, particularly when considering the anticipated photon rates from the faint weak laser source operating in the high kHz and MHz frequency ranges.

Lastly, one can conclude from the investigation of the DCR of channel 1, that all further measurements have to be done at a bias current of $I_B \approx 31.2\mu\text{A}$. As mentioned above the final figure of merit for the DCR is depending on the bias current working point. In this work, five 60s measurements were done for three different bias currents (24 , 28 and $31.2\mu\text{A}$).

The averaged results for channel one of the detector yield a DCR of:

$$DCR_{24\mu\text{A}} = (1.40 \pm 1.02)\text{Hz} \quad (4.1)$$

$$DCR_{28\mu\text{A}} = (1.20 \pm 0.98)\text{Hz} \quad (4.2)$$

$$DCR_{31.2\mu\text{A}} = (1.40 \pm 1.36)\text{Hz} \quad (4.3)$$

where the error is the standard deviation of the mean.

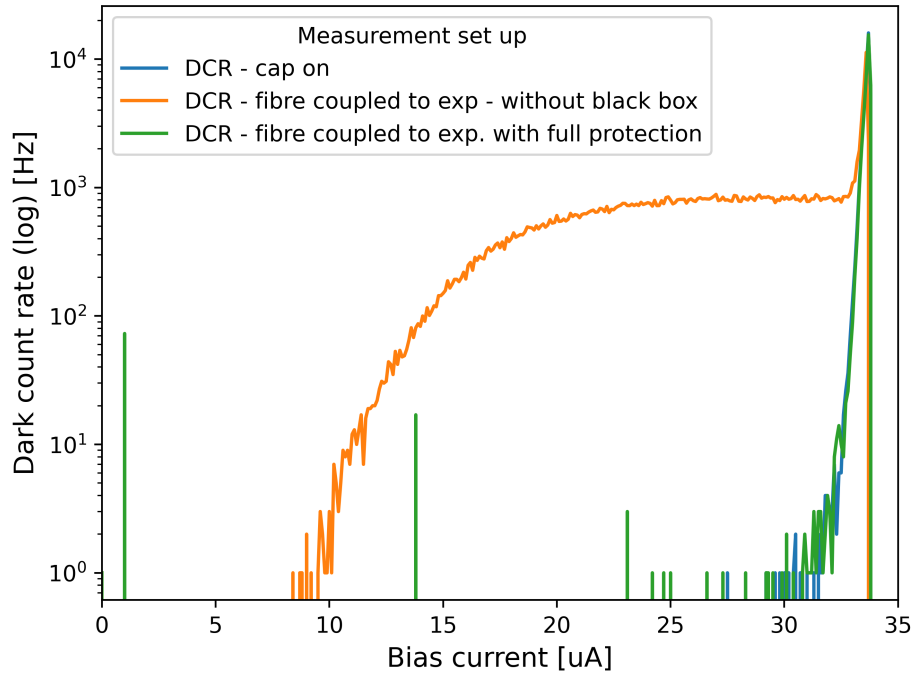


Figure 4.1: Channel 1 DCR measurements for different bias currents at a trigger voltage of 200MHz. The blue curve shows the DCR with a cap on the output port of the detector. The orange curve shows the DCR with a fibre connected to the detector and the fibre output coupling of the experiment. The green curve shows the DCR with a fibre connected to the detector, the fibre output coupling of the experiment and alumini foil wrapped around the optical fibre.

4.2 Recovery time

The concept of the recovery time is visually depicted in fig 4.2. When a photon hits the detector and is absorbed, the efficiency of the detector drops to zero and no further photons can be measured for a certain period of time. This elapsed time is called the dead time $\tau_{\text{dead}} = \tau_d$. The efficiency then rises again to the original device efficiency η_G . This period is called the reset time $\tau_{\text{reset}} = \tau_r$. The vertical dashed line forms the starting point where the efficiency rises again to the original device efficiency η_G . Finally, the sum $\tau_{\text{rec}} = \tau_r + \tau_d$ of both times forms the recovery time τ_{rec} .

The recovery time is important because it determines the rate the detector can detect photons. The lower the recovery time, as higher the counting rate.

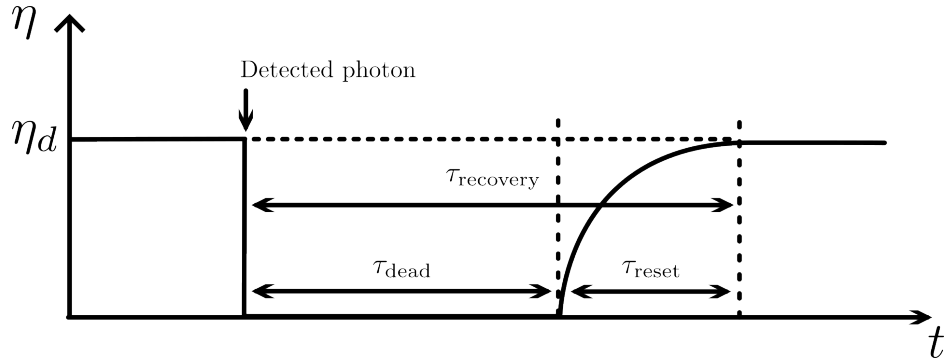


Figure 4.2: Schematic efficiency curve for the detection of a photon[10]. On the Y axis is the efficiency η , where η_{dde} is the device efficiency. On the X axis is the time course of the efficiency The trajectory of the initial device efficiency, represented by the variable , does not align with the illustration

Measurement and results

In this work, the recovery time of the detector is determined through an autocorrelation method based on a continuous wave laser source (a faint laser source), a technique that has been previously employed by other research groups. [11, 12]. The measurement was conducted with the setup shown in fig 4.3. The raw analog signals from the detector were directly transmitted to a time tagger unit (Time Tagger 20) by Swabian instruments. with self-adjustable trigger voltages, a device deadtime of 6ns and a maximal counting rate of 9MHz.

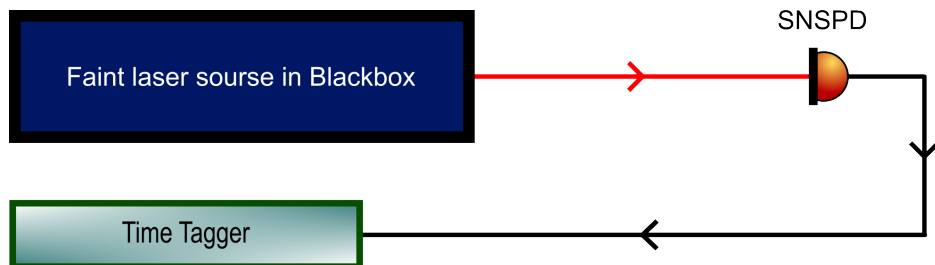


Figure 4.3: Experimental setup for measuring the recovery time. Optical setup of "faint laser source in black box" is depicted in 3.1

This unit enabled the tagging of incoming signals with a time tag, as implied by its name. Subsequently, the tags were used to process the time distances between all signals. The histogram of these distances provide an autocorrelation in time (here not normalized). The autocorrelation was measured for one channel for four different bias currents ($25\mu\text{A}$, $27\mu\text{A}$, $29\mu\text{A}$ and $31.2\mu\text{A}$) and trigger voltages from 300mV to 900mV in 100mV steps.

These measurements were done to determine the recovery time and analyze it dependencies. The results for a fixed bias current of $31.2\mu\text{A}$ are shown in figure 4.4(a) and for $26\mu\text{A}$ in 4.4(b). The other measurement results are presented in the appendix ??.

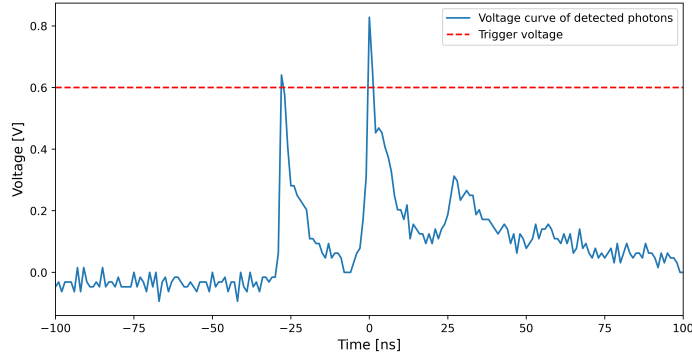


Figure 4.5: Analog signal of three consecutive pulses recorded with an oscilloscope with trigger at 600mV. f Detector was set up to a bias current of $31.2\mu\text{A}$ and the faint laser source was attenuated down to ≈ 0.5 MHz. The time resolution of the oscilloscope was 200MHz.

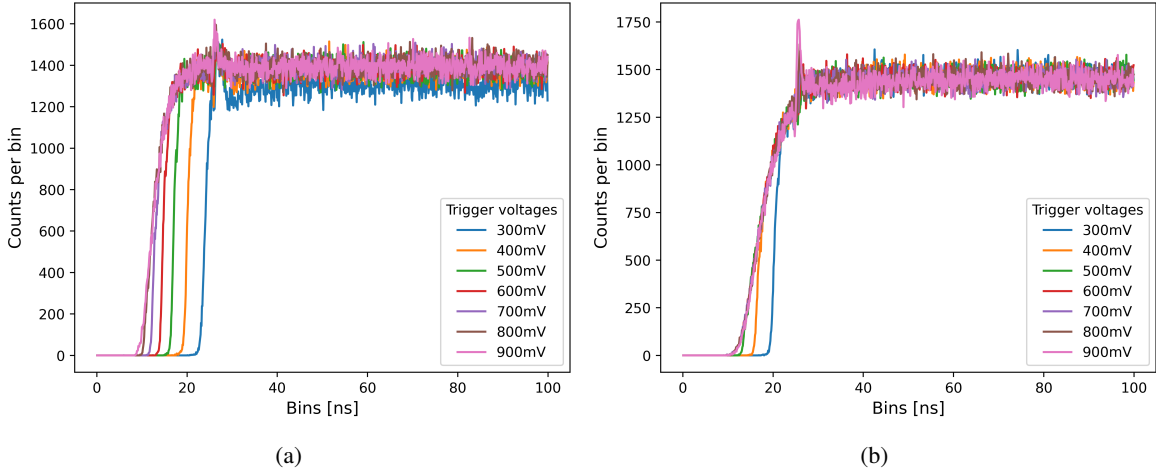


Figure 4.4: Autocorrelation of distances between two photon detection events for (a) $I_B = 31.2\mu\text{A}$ and (b) $I_B = 25\mu\text{A}$. The X-axis represents the time distance between two signals in 1ns steps and the Y-axis the counts per bin.

The results of the autocorrelation show three major features. First, for low trigger voltages, the dead time is longer and decrease for increasing trigger voltages. This is true for both, the lower and higher bias current. The reason for this behavior can be explained best by looking at an exemplary raw analog signal (see fig 4.5) of two consequent pulses. In figure 4.5 one can see the peaks of two consecutive detection signals, where the second pulse starts ($\approx 20\text{ns}$) before the falling edge of the first pulse ends. Physically, that means, that before the first signal spike has fully decayed a second photon, already hit the detector, got detected and produced a second spike.

If the trigger is below 500mV the time tagger will count this signal as one count, since the second pulse came when the remaining voltage of the wire was above 500mV. If the trigger is above 500mV both pulses will be counted. This allows successive events with smaller time delay between them and therefore reduces the perceived recovery time.

Secondly, for the lower bias current ($26\mu\text{A}$), the rising count curves for each trigger voltage converge

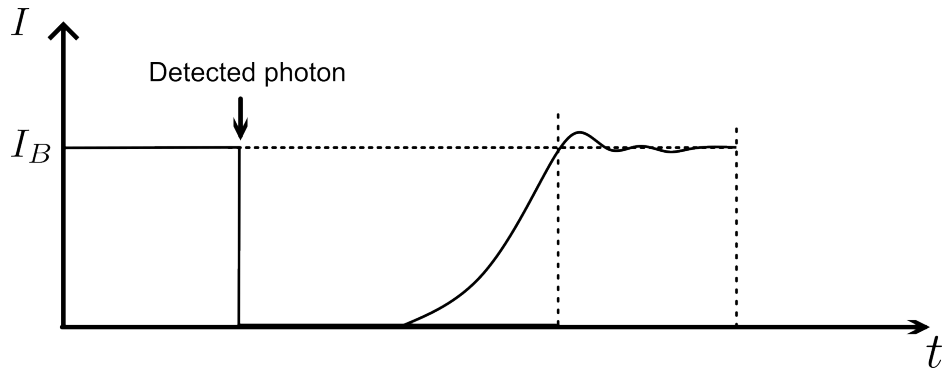


Figure 4.6: A sketch of the assumed bias current behaviour is presented herewith. Once the bias current has been reached, the current undergoes a brief oscillation before stabilising at the bias current level.

earlier in comparison to the bias current of $31.2 \mu\text{A}$. At the bias current of $31.2 \mu\text{A}$, the four different count curves remain distinct until they reach their peak. This can be attributed to the differing pulse heights, dependent on the bias current. According to Ohm's law, for the same resistivity, a lower bias current corresponds to lower voltage pulses and vice versa. Due to the lower pulse, the regime, where pulses can be resolved by a trigger voltage of 600mV but not 500mV becomes smaller. The different pulse heights can also be verified by the recorded analog signals shown in figure: ??.

The third interesting feature is the count peak at $24\text{-}27\text{ns}$ for $31.2\mu\text{A}$ and a trigger level of 300 mV 4.4(a).

This small peak is less visible at lower bias currents or higher trigger levels. Closer examination of this trend are shown in the appendix A.

This behavior can be understood by taking into account that the bias current needs a finite amount of time to reach its target value once the superconductivity is restored and will also overshoot a bit after reaching the target value. A sketch of the expected behavior is shown in figure 4.6.

Following the detection of a current, the course of the current does not proceed directly and precisely to the bias current. Instead, it oscillates for a brief period and then rapidly reaches equilibrium.

If the target bias current is close to the critical current the overshooting might cause a breaking of the superconductivity leading to a time correlated increase in the dark current rate (seen in figure 4.1). This feature is less severe for higher trigger voltages which suggests that the self triggered pulse is typically of smaller height.

It can be concluded that the optimal recovery time is achieved when the detector is operated at a bias current maintained at a level that is close but not excessive to critical current of $31.2\mu\text{A}$ and a trigger voltage of 600v .

This enables the generation of a higher pulse, which in turn results in a steeper reset time, a shorter dead time, and consequently, a shorter recovery time.

Finally, a reasonable trigger point for a bias current of $31.2\mu\text{A}$ is 600mV , since it yields the best compromise between a short recovery time and a low additional oscillation signal as discussed above. The calculation of the τ_{rec} is done by measuring 10 times the autocorrelation this configuration. Afterwards, bin values of analog bins are averaged and the error is calculated by the standard deviation. The recovery time is then calculated by calculating the average of counts per bin from $28\mu\text{A}$ till the end of the measurement period first. This point is chosen as the starting point, because from this point a constant curve, hence maximal detection efficiency is assumable (saturation value). Based on this

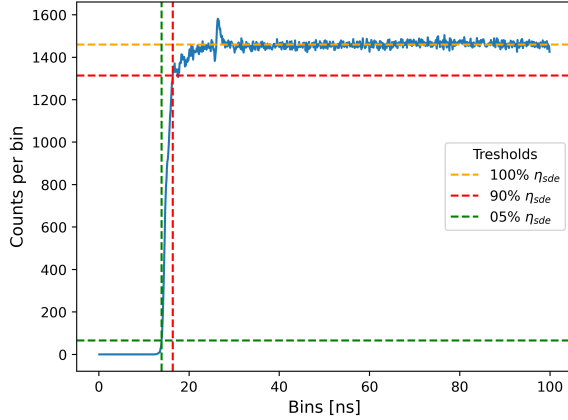


Figure 4.7: Autocorrelation of averaged distances between two photon detection events for $I_B = 31.2\mu\text{A}$ and 600mV. The X-axis represents the time distance between two signals in 1ns steps and the Y-axis the countsper bin. H- and v-lines indicate the dead-; reset- and recovery time.

saturation value a 05%, 50% and 90% threshold is calculated. The threshold is then used to define the dead time τ_{dead} as the time, where the detector is reached 05% of the saturation value. Furthermore, the reset time τ_{reset} is defined as the time from 05% till 90% of the saturation value. The calculated points are visualized in figure: 4.7. The recovery time is then calculated by the total value of the dead and reset time $\tau_{\text{rec}} = \tau_{\text{dead}} + \tau_{\text{reset}}$. Errors are calculated by using the mean root square of the time values of the corresponding standard deviation of the bin value.

$\tau_{\text{rec}}^{90\%} = (17.156 \pm 0.0445)\text{ns}$ for $I_B = 31.2\mu\text{A}$ and 600mV, where $\tau_d = (13.950 \pm 0.050)\text{ns}$ is the dead time and $\tau_r = (3.206 \pm 0.447)\text{ns}$ the reset time. Moreover, the time the detector is back at efficiency of $\eta_{\text{sde}} = 50\%$ is $\tau^{50\%} = (14.900 \pm 0.0816)\text{ns}$

4.3 Efficiency

There are three types of efficiencies that describe independent loss processes in single photon detection. Efficiency is a way of measuring how likely a process is to happen. There are three main types of efficiency: the coupling efficiency (η_C), the absorption efficiency (η_A) and the registration efficiency (η_R). The graph 4.8 shows schematically where the different losses in the detection process appears. When a photon is sent to a detector via an optical fibre, not all photons can be coupled into the fibre. The probability of coupling is the so called the *coupling efficiency*. When photons hit the detector, there is always a probability that the photon will not be absorbed by the detector. This is due to material and symmetry properties like the design of the superconducting nanowire [8]. This is described by the *absorption efficiency*. Finally, there is always a probability that the photon will not be registered by the measuring electronics. This is expressed with the *registration efficiency*.

In literature, these terms are summarized in two general efficiency terms: the device detection efficiency ($\eta_{\text{dde}} = \eta_A \cdot \eta_R$) and the system efficiency ($\eta_{\text{sde}} = \eta_A \cdot \eta_R \cdot \eta_K$) [2, 8]. The device detection efficiency η_{dde} corresponds to the efficiency of the device itself and neglects coupling inefficiencies. This gives an idealized upper bound to the achievable efficiency. For perfect optical coupling, the device detection efficiency is equal to the system detection efficiency ($\eta_{\text{dde}} = \eta_{\text{sde}}$). The system

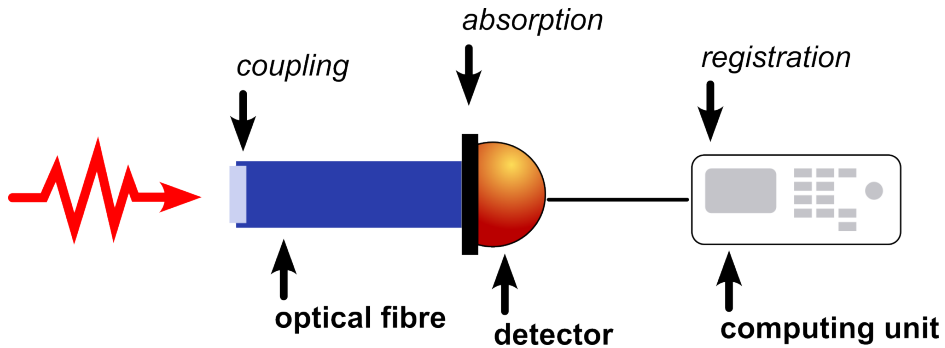


Figure 4.8: Sketch of the components in the detector setup where photonlosses appear and consequently a probability (η_K , η_A or η_R) has to be considered.

detection efficiency η_{sde} takes the coupling losses to the optical fibre into account. This is the case if the detector is connected to a fibre, as the device properties or the experiment does not allow photon detection in a free environment.

Measurement and results

In the given setup, only the system detection efficiency η_{sde} is measured, because the detector is already prebuild with a fixed coupling to a fibre [3]. This internal fibre is connected to a single mode fibre to fibre port for the connection type FC/PC (fibre channel / physical contact). Through this, one can connect the detector with an external optical fibre and send photons from the experiment to the detector.

The system detection efficiency η_{sde} will depend on the applied bias current, the chosen trigger voltage and the photon rate and the photon polarization. Here, all these dependencies will be investigated to characterize the system detection efficiency. Each measurement was done in the setup explained in part 3.

Polarization dependency

The measurements were done in a specific order, since the conclusions drawn for certain measurements influence the preceding measurements. Based on this, it is first necessary to align the polarization of the laser light with the slow axis of the fibre connected to the output port of the detector. According to the manual the coupled light needs to be polarized along the slow axis of the fibre [3]. This is explained by the fact that the absorption efficiency η_A is maximized when the light is polarized parallel to the superconducting nanowire of the detector as explained in 2.

A combination of a quarter-wave plate and a half-wave plate is used to alter the polarization of the input laser light. The quarter-wave plate is used to pre compensate the stress induced birefringence of the fiber input while the half-wave plate is used to rotate the linear input polarization. The measurement of the polarization was done with the polarization analyzer SK010PA by Schäfer + Kirchhoff. Furthermore, the laser power input was set to $511.1 \mu\text{V}$, corresponding to a photon rate of 2.006 PHz, and attenuated by three ND filters with a total OD of 9.574, in order to make sure that the detector can reach high count rates as considered in 3.2. Different polarization angles for measuring

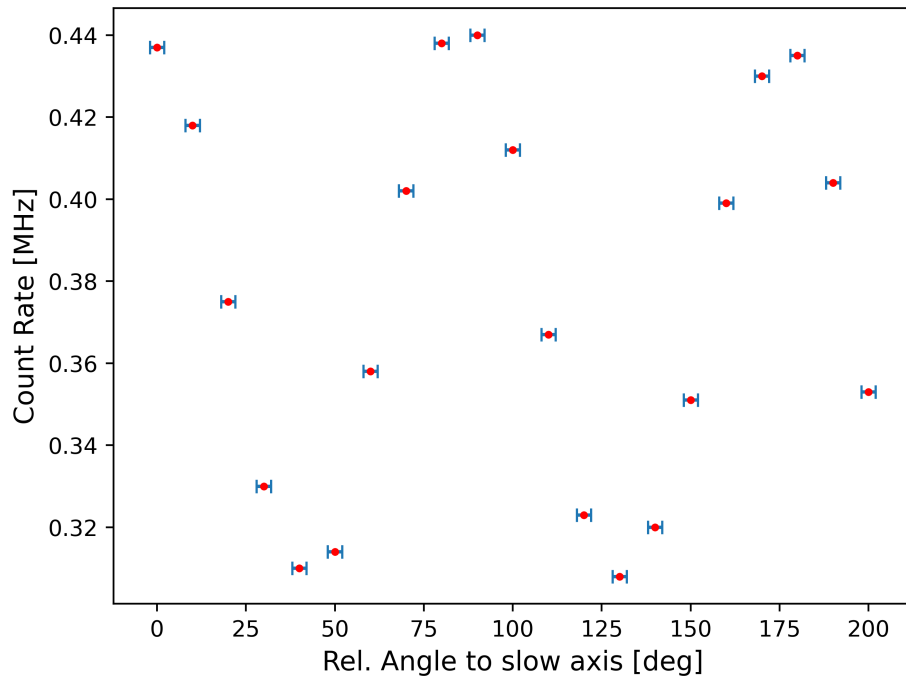


Figure 4.9: On the X axis the relative angle to the slow axis is depicted with an estimated error of 2° . The Y axis shows the angle dependent count rates. Countrate error are depicted in table A.2 and calculated according considerations mentioned in ??

the countrate of the detector are then realized by rotating the half-wave plate while the quarter wave plate is kept in its position. Final alignment of the polarization are shown in the Appendix A.3.2.

By adjusting the laser beam linear with a quarter-wave plate first and rotating the half-wave plate in $(10 \pm 2)^\circ$ steps afterwards, the polarization axis was rotated relative to the slow axis of the fibre. With this, it was possible to find the angle configuration were the maximum of light was coupled to the slow axis of the fibre. This is important since measuring subsequent efficiency measurements aligned to a different axis would put a systematic downshift on the true efficiency of the detector. In the figures 4.9 the count rates are depicted. For preceding measurements the polarization was aligned to the relative angle of $(0 \pm 2)^\circ$, where the maximum count rate was reached.

From now on for the following measurements, the polarization angle which yields the highest efficiency was used.

Trigger voltage and bias current dependency

In a second measurement the trigger voltage and bias current dependency was investigated for different count rates. For this measurement a different power as input was used because the power drifted over time and could not be reproduced to the power level used in the polarization alignment. The new power level was set to $518.1\mu\text{V}$, corresponding to a photon rate of 2.034 PHz . Furthermore, the ND filters were used for attenuation to reach different count rates in the MHz regime.

In order to investigate the trigger voltage and bias current dependency the bias current was swept from 0 to $35\mu\text{A}$ in $0.1\mu\text{A}$ steps, and events within 1s integration time were counted.

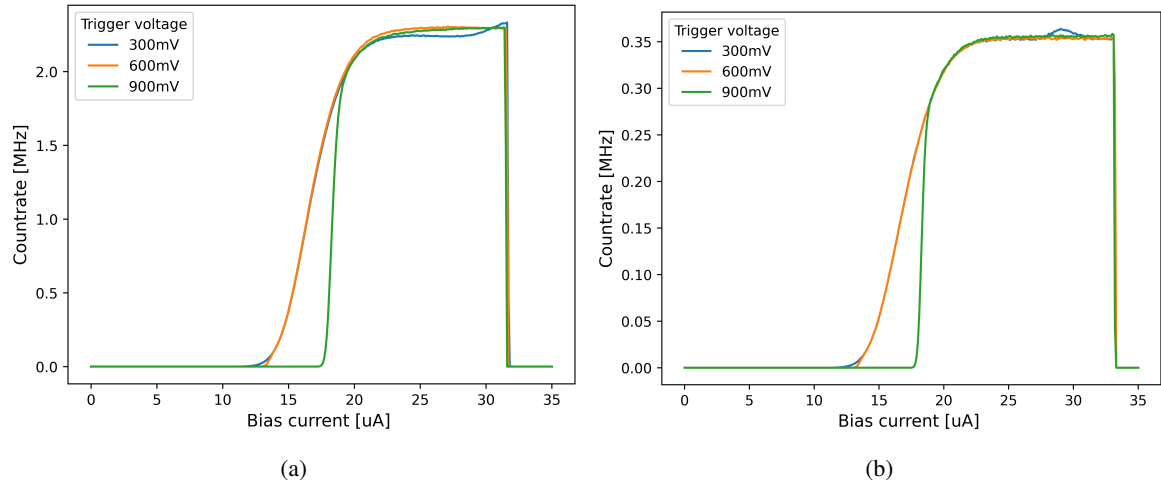


Figure 4.10: Count rates for different bias currents and trigger voltages. The count rates are measured for a trigger voltage of 300mV, 600mV and 900mV. (a) shows the measured count rates for an input count rate of 2.45MHz and (b) for 0.39MHz. Curve for a trigger voltage of 300mV and 600mV are laying on each other and are not distinguishable in the lower bias current regions.

In figure 4.10(a) and 4.10(b) one can see that at lower trigger voltage of 300mV the count rate oscillates a bit, which again likely corresponds to the increased dark count rates as explained in 4.6. Furthermore, one can see that for lower trigger voltages the detected counts for lower bias currents are higher. This corresponds to the detection of lower voltage pulses in lower bias current regimes if the trigger voltage is low. Another behaviour is the saturation, where the count rate stays constant, which is reached independent of the trigger voltage, at around $I_{Bias} \approx 20\mu A$. At the end of the curve, for the higher count rate (a) the counting of the detector drops a bias current of $I_{Bias} \approx 32\mu A$ and for the lower count rates at $I_{Bias} \approx 34\mu A$. One can assume that the critical current is reached earlier when more photons are send to the detector, because the nanowire is not able to recover that fast enough. Overall, one can conclude that the behaviour of the count rates does not change significantly for the trigger voltage of 600mV and 900mV.

One interesting additional observation is that if the count rate is reached a certain amount, the voltage peak is decreasing, tough the voltage peak of the analog signal is raising, when the Bias current is increased. This can be seen in the comparison 4.11 of the recordings of the voltage pulses with the same bias current and trigger voltage but different count rates. Moreover, if several photons are detected in the same time, the voltage peak is highly fluctuating. This is observable in the comparison in the three consecutive pulses in figure (b).

This behaviour is can be backed with the lower count rates for higher trigger voltages in figure ?? at the bias sweep measurements A.5. One possible explanation for this phenomenon is that the hotspot in the nanowire has not been entirely dissipated, resulting in incomplete restoration of the initial superconductivity

Therefore, the optimal and maximum trigger voltage is a function of both the bias current and the photon rate being sent to the detector. A midpoint trigger voltage of 600 mV is reasonable when measuring with a count rate in the 100 kHz regime. For higher count rates, a reduction in the trigger voltage may be appropriate; however, this may result in an increased risk of detecting noise signals,

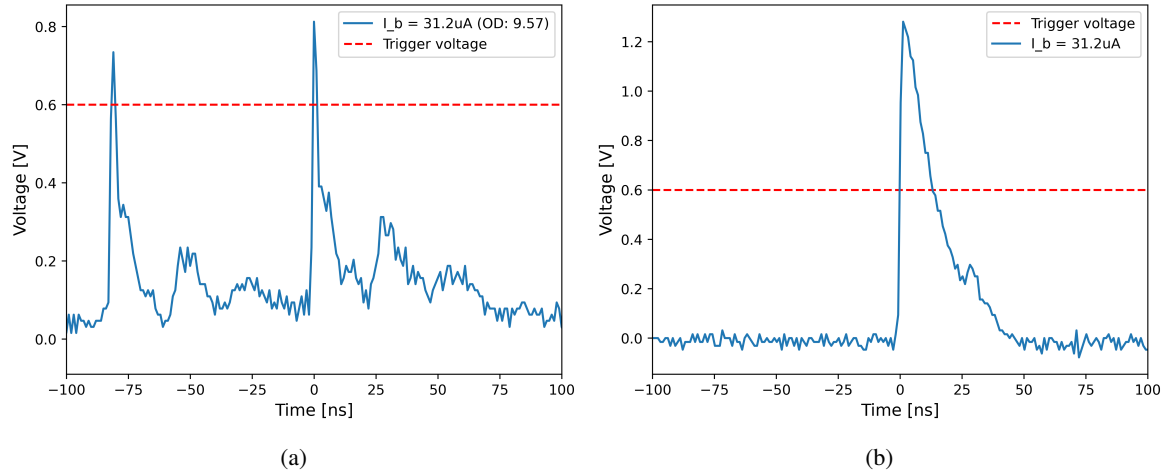


Figure 4.11: Analog voltage pulse signals for the count rates 547.546KHz (a) and 1.771KHz (b). In both recordings the same bias current $I_b = 31.2\mu\text{A}$ and trigger voltage 600mV is used. In (b) at $\approx 26\text{ns}$ minor peak on the descending curve is visible. This may be attributed to back reflection in the cable.

such as cable back reflection seen in (b), as photon count.

Input count rate dependency

Finally, efficiency measurement for different count rates were done, to determine the bandwidth where photons are detected with the highest efficiency. The count rates were varied by using different ND filters and was done by putting together different ND filter combinations in order to get 6 different count rates (0.39MHz, 0.78MHz, 1.391MHz, 1.771MHz, 2.401MHz, 2.45MHz). To avoid the oscillation of count rates near the critical current as seen in the blue curve in figure 4.10(a) and 4.10(b) a trigger voltage of 600mV is used. Further, the bias current was set to $31.2\mu\text{A}$ for each configured count rate. However, with this bias current configuration it is not possible to measure higher count rates than 2.401MHz (OD = 8.928), due an earlier breakdown of counting, due to the failing recovery of the superconducting nanowire.

For each of the 6 input count rates the detected count rate was measured for 30s with an integration time of 1 second. This measurement was repeated 5 times. Afterwards, the system detection efficiency η_{sde} was calculated by the formula $\eta_{\text{sde}} = \frac{N_{\text{detected}}}{N_{\text{sent}}} \cdot 100$. Where N_{detected} are the averaged count rate of the 5 measurements and N_{sent} is the input count rate, calculated via the OD of the ND filters and the photon number per second of the initial laser power $N_{\text{sent}} = N_{\text{sent}} \cdot 10^{-\text{OD}}$. The resulting 6 efficiency values are plotted vs the input count rates 4.12 and can be seen in table ??.

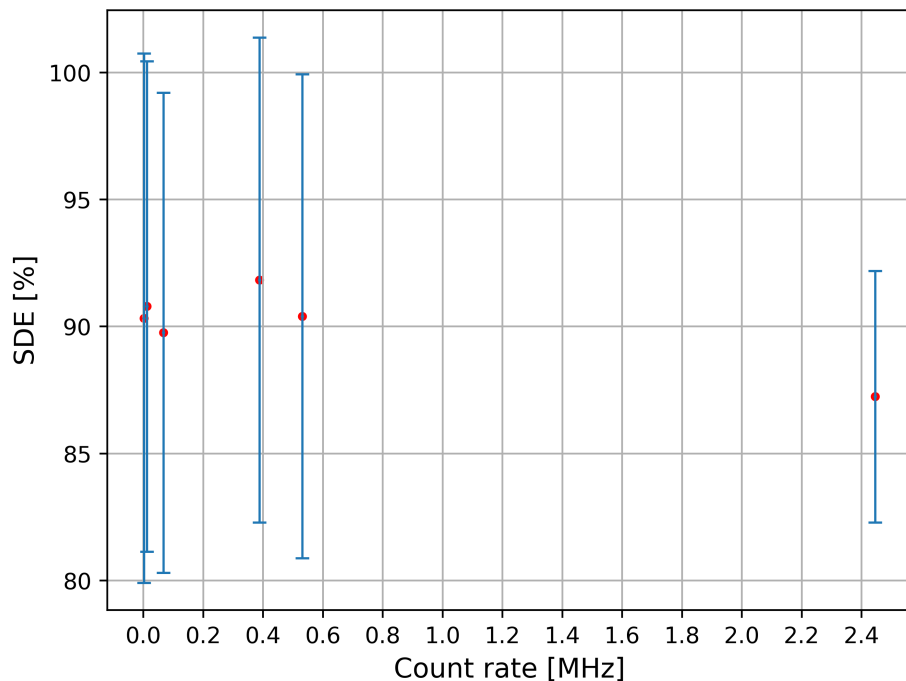


Figure 4.12: System detection efficiency appears in a range between $(87.242 \pm 4.955)\%$ and $(91.834 \pm 9.550)\%$. Errors are calculated according to A.1 and due to the high uncertainty in the OD calculation unphysical values of over $\eta_{\text{sde}} = 100\%$ are included in the error range.

In figure 4.12 one can not see the expected clear downward trend for higher count rates. In order to investigate the bandwidth of η_{sde} further, bias sweep measurements were done for two further higher count rates (67.363MHz and 9.575MHz). Afterwards, the point with the highest count rates, hence $\eta_{\text{sde max}}$ were compared and displayed again vs the input count rates.

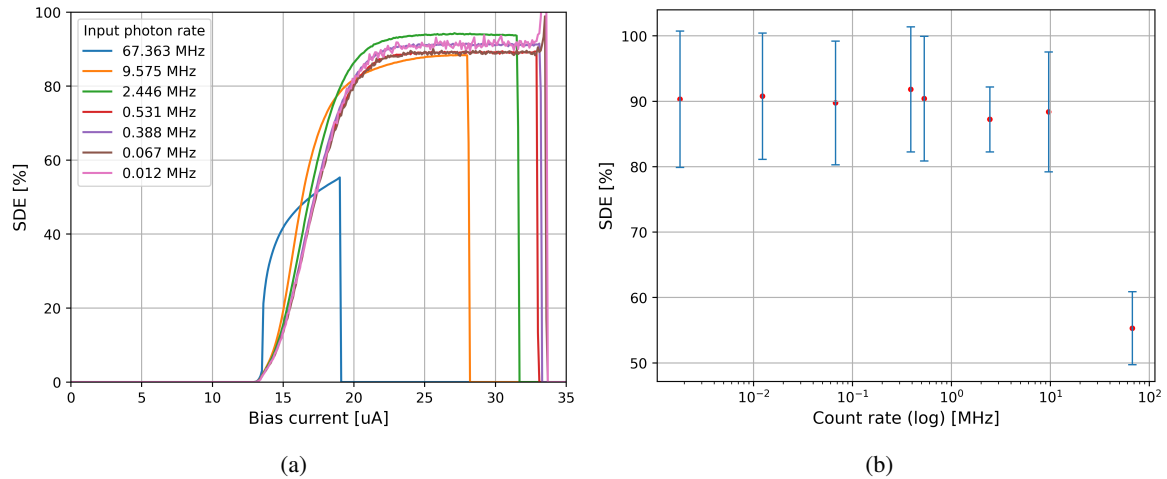


Figure 4.13: (a) curves of system detection efficiency for different bias current. Curve for 0.39MHz was left out because the high relative fluctuations made the other curves unreadable. The raising edges at the end of the curve are due to the rising noise, as already seen in 4.1 In (b) curve of system detection efficiency for two further higher count rates plotted on logarithmic X - axis to emphasize the efficiency bandwidth.

In figure 4.13(a) one can clearly see two different behaviours. First, for higher count rates the maximal bias current the detector can handle is reached earlier and no constant count rate is reached. This dynamics follows from the fact that the detector is not able to recover in time, when the count rate is too high. Hence, the critical temperature is reached earlier, when the count rate is raising and the detections is shut down. This makes the counting process highly unstable and unreliable, especially if one want to measure with the highest possible count rate, which appears close to the edge of the breakdown.

Secondly, the system detection efficiency η_{sde} is decreasing for higher count rates. Moreover, the measurement shows the constant efficiency for count rates lower than the set 2.45MHz. The maximal system detection efficiency of $\eta_{\text{sde}} = (91.834 \pm 9.550)\%$ was measured at a count rate of 1.391 MHz.

4.4 Discussion

Discussion - Dark count rates

Measurement confirms fabric values

Discussion - Recovery time

Recovery, dead and reset time are in the expected range. Small oscillation has considered if measurement happens for single photon source with this time distance between each photon.

Discussion - Efficiency

Every efficiency measurement confirms the expectation. average efficiency for a bandwidth of 10MHz is 89 percent. Company did efficiecy measurements for this channel and got 87 pm 3 percent.

Some further consideration regarding the source of the sinking efficiency for higher count rates.

Unmeasurable Photons due to the dead time

Further, as introduced in 2, with the calculated dead time from 4.2 the average photon rate \bar{n} per length segment L_d is calculated. Calculations show that the dead time length segment yields a length of $L_d = (4.185 \pm 0.015)\text{m}$. To calculate the average photon rate per length segment, one has to consider the photon flux Φ . Since the photon flux is varied later, the average photon rate with the two highest photon flux will be considered first. The highest photon flux is used when the lowest attenuation with $\text{OD} = (7.482 \pm 0.100)$ and $\text{OD} = (8.327 \pm 0.104)$ is used. This gives an upper bound of $\Phi = 67.078\text{MHz}$ and $\Phi = 9.594\text{MHz}$. The resulting average photon rate per length segment is then $\bar{n} = 0.936 \pm 0.095$ and $\bar{n} = 0.134 \pm 0.014$. This yields according to the probability of the poisson distribution

$$P_{\text{dead}}^{7.482}(n < 2) = 0.172 \quad (4.4)$$

$$P_{\text{dead}}^{8.327}(n < 2) = 0.013 \quad (4.5)$$

for having two photons in our length segment L_d . Theoretically, errors on for poisson distribution are calculated by $\Delta n = \sqrt{n}$. However, those errors have low validity, since implicate possible values lower than zero and contradicting the fact their can not be less than 0 photons per length segment.

This gives an amount of

$$N_{\text{lost}} = P_{\text{dead}}^{7.482}(n < 2) \cdot 67.078\text{MHz} = 16.098\text{MHz} \quad (4.6)$$

$$N_{\text{lost}} = P_{\text{dead}}^{8.327}(n < 2) \cdot 9.594\text{MHz} = 0.125\text{MHz} \quad (4.7)$$

we inherently can not detect, because photons are too close to each other.

Due to the fact that the probability of $P_{\text{dead}}^{8.327}(n = 2) = 0.013$ is already low, those considerations for lower count rates $\Phi < 9.594\text{MHz}$ will be neglected.

However, here one has to consider, as calculated in 4.4, that there is an amount of photons which is not detectable because their time distance to each other is less than the dead time. When subtracting the two calculated unmeasurable photon rates from the input count rates

$$\eta_{\text{sde}}^{\text{adjusted}} = 67.078 - 16.098 = 50.980\text{MHz} \quad (4.8)$$

$$\eta_{\text{sde}}^{\text{adjusted}} = 9.594 - 0.125 = 9.469\text{MHz} \quad (4.9)$$

and considering the η_{sde} of the photons left to be detected, one gets the following new system detection efficiency values:

$$\eta_{\text{sde}}^{\text{adjusted}} = (73.085 \pm 5.581)\% \quad (4.10)$$

$$\eta_{\text{sde}}^{\text{adjusted}} = (89.375 \pm 9.149)\% \quad (4.11)$$

CHAPTER 5

Conclusion and Outlook

APPENDIX A

Appendix

A.1 ND filter calibration

To calculate the OD value of the ND Filters, we have to consider the statistical error from the transmission value and the systematic error, we get from measuring the OD with two methods, as explained in [3.2](#).

We first consider the statistical error from the transmission value. The transmission value is defined as:

$$T = \frac{P_{\text{ND}}}{P} \quad (\text{A.1})$$

Where P is the power detected by the power metre without the ND filter and P_{ND} is the power we measured with applied ND filter.

For the Error calculation the following considerations are done:

First, for both P and P_{ND} the measurement uncertainty of the photodiode from the photodiode is always 3% of the measured value [\[13\]](#). Since this uncertainty does not affect the overall relation between the two measurements it does not contribute to the error calculation. However, the measurement uncertainty from reading the value from the Powermeter contributes to both, P and P_{ND} , since reading the value from the powermeter provides always a different error because the last displayed order of magnitude of the displayed result on the powermeter fluctuates.

Further, regarding ΔP it is also important to mention that after each ND filter change, the coupling was readjusted to the maximal vale. However, after the ND filter was removed it was not possible to get to the same initial value. Therefore, we always have different power values we compare, though the filtering process was done always with the same fixed laser power setting. Based on this, P is the mean value of all initial values was taken and for the error the standard deviation was calculated. Due to this we have also to consider an *additional error source* ΔP^{STD} from the fiber coupling and optimization in ΔP .

Important: This only applies for the first measurement method because we adjust there our fiber coupling. In the second measurement we have a stable P because there, the fiber coupling was not adjusted, once the maximum was reached.

So, ΔP for the first measurement method is calculated as follows:

Appendix A Appendix

$$\Delta P = \sqrt{(\Delta P_{\text{Read off}})^2 + (\Delta P_{\text{STD}})^2} \quad (\text{A.2})$$

For P_{ND} applies $\Delta P_{\text{ND}} = \Delta P_{\text{Read off}}$

As result we get the following error for the transmission rate:

$$\Delta T_{\text{stat}} = \sqrt{\left(\frac{\Delta P_{\text{ND}}}{P}\right)^2 + \left(\frac{\Delta P P_{\text{ND}}}{P^2}\right)^2} \quad (\text{A.3})$$

In the following the table with the measurement values and results for the Transmission value and its corresponding statistical error is shown:

ID	T_{measured}	ΔT_{stat}
TP0333766	1,43E-01	3,223E-03
TP03337667 (2)	1,47E-01	3,073E-03
TP03366490	8,26E-03	1,882E-04
TP03366490 (2)	7,93E-03	1,744E-04
TP03275234	1,00E-03	4,381E-05
TP03312353	1,04E-03	4,312E-05
TP03271009	1,02E-03	4,432E-05
TP03275234 (2)	1,03E-03	4,303E-05
TP03324728	1,80E-04	3,843E-05
TP03287742	1,78E-04	3,731E-05
TP03348187 (2)	1,82E-04	3,921E-05
TP03348187	1,82E-04	3,862E-05

Table A.1: Results for the transmission rate and its statistical error. The ID is the identification number of the OD filter.

ID	OD_{expected}	T_{measured}	T Value Error Systematic	T Value Error stat	T Value Error	Mean OD Value	OD Value Error
TP03337667	1,00	1,43E-01	67,697E-4	3,223E-03	7,50E-03	0,844	0,023
TP03337667 (2)	1,00	1,47E-01	50,474E-04	3,073E-03	5,91E-03	0,832	0,017
TP03366490	3,00	8,26E-03	32,418E-05	1,882E-04	3,75E-04	2,083	0,020
TP03366490 (2)	3,00	7,93E-03	52,291E-05	1,744E-04	5,51E-04	2,101	0,030
TP03275234	4,00	1,00E-03	5,318E-05	4,381E-05	6,89E-05	2,999	0,030
TP03312353	4,00	1,04E-03	7,142E-05	4,312E-05	8,34E-05	2,983	0,035
TP03271009	4,00	1,02E-03	4,842E-05	4,432E-05	6,56E-05	2,991	0,028
TP03275234 (2)	4,00	1,03E-03	6,566E-05	4,303E-05	7,85E-05	2,986	0,033
TP03324728	5,00	1,80E-04	9,945E-06	3,843E-05	3,96E-05	3,744	0,095
TP03287742	5,00	1,78E-04	4,196E-06	3,731E-05	3,75E-05	3,749	0,092
TP03348187 (2)	5,00	1,82E-04	4,506E-06	3,921E-05	3,95E-05	3,739	0,094
TP03348187	5,00	1,82E-04	5,792E-06	3,862E-05	3,91E-05	3,739	0,093

Further for calculating the total transmission value and its error, we have to include the measurements and errors for the second method. Here, we have a stable P because the fiber coupling was not adjusted, once the maximum was reached. The transmission error for the second method is calculated as follows:

$$\Delta T = \sqrt{\left(\frac{\Delta P_{\text{ND}}}{P}\right)^2 + \left(\frac{\Delta P P_{\text{ND}}}{P^2}\right)^2} \quad (\text{A.4})$$

Both ΔP_{ND} and ΔP are estimated by the read off error of the powermeter.

With booth transmission values, the total transmission value and its error can be calculated as follows:

$$T_{\text{total}} = \frac{T_{\text{stat}} + T_{\text{systematic}}}{2} \quad (\text{A.5})$$

$$\Delta T_{\text{total}} = \sqrt{\Delta T_{\text{stat}}^2 + \Delta T_{\text{systematic}}^2} \quad (\text{A.6})$$

Continuing with the calculation of the OD value, we have according to [14] the relation: $\text{OD} = \log\left(\frac{1}{T}\right)$. From this, we can calculate the error for the OD: $\Delta \text{OD} = \frac{\Delta T}{\ln(10) \cdot T}$

The resulting power after stacked ND filters are calculated as follows:

$$P_{\text{ND}} = P \cdot 10^{-\text{OD}} \quad (\text{A.7})$$

The corresponding error is $\Delta P = 0.03 \cdot P$ and hence the total error for the power after the ND filter is calculated as follows:

$$\Leftrightarrow \Delta P_{\text{ND}} = \sqrt{(\Delta P \cdot 10^{-\text{OD}})^2 + (P \cdot \log(10) \cdot \Delta \text{OD})^2} \quad (\text{A.8})$$

An additional error from reading off the count rate (hence, the corresponding Power) from the computer screen was also considered, since measurement with the power metre was not able. However, because the fluctuating rate of the count rate was in the order of a few Hz, it was neglected for the final error calculation.

Appendix A Appendix

Table A.2: Angle Dependent countrate results

Table A.3: Angle Dependent SDE Results

A.2 Angle dependent countrate and η_{sde}

A.3 Recovery time measurements

A.3.1 Recovery time measurements - Oscillating bias current

A.3.2 Polarization alignment for system detection efficiency measurements

A.4 Recordings of analog pulses

A.5 Bias sweeping for different count rates

In the appendix you usually include extra information that should be documented in your thesis, but not interrupt the flow.

Bibliography

- [1] G. N. Gol'tsman et al., *Picosecond superconducting single-photon optical detector*, *Applied Physics Letters* **79** (2001) 705, URL: <https://doi.org/10.1063/1.1388868>.
- [2] C. M. Natarajan, M. G. Tanner and R. H. Hadfield, *Superconducting nanowire single-photon detectors: physics and applications*, *Superconductor science and technology/Superconductor science technology* **25** (2012) 063001, URL: <https://doi.org/10.1088/0953-2048/25/6/063001>.
- [3] Single Quantum, *Single Quantum EOS User Manual*, 2022.
- [4] G. A. Steudle et al., *Measuring the quantum nature of light with a single source and a single detector*, *Physical review. A, Atomic, molecular, and optical physics/Physical review, A, Atomic, molecular, and optical physics* **86** (2012), URL: <https://doi.org/10.1103/physreva.86.053814>.
- [5] singlequantum.com, *Superconducting Nanowire Single Photon Detectors Operation principle*, <https://singlequantum.com/wp-content/uploads/2023/06/Single-Quantum-Operation-Principle-print.pdf>, Accessed: 2023-06, n.d.
- [6] F. Zheng et al., *Design of a polarization-insensitive superconducting nanowire single photon detector with high detection efficiency*, *Scientific reports* **6** (2016), URL: <https://doi.org/10.1038/srep22710>.
- [7] Single Quantm, *Operation principle of SNSPD*, URL: <https://www.singlequantum.com/technology/snspd/> (visited on 25/07/2024).
- [8] R. H. Hadfield, *Single-photon detectors for optical quantum information applications*, *Nature photonics* **3** (2009) 696, URL: <https://doi.org/10.1038/nphoton.2009.230>.
- [9] Wikipedia contributors, *Signal-to-noise ratio*, 2024, URL: https://en.wikipedia.org/wiki/Signal-to-noise_ratio.
- [10] K. Shalm et al., *Single-Photon Detector Tutorial*, Computer Scientist QCRYPT, National Institute of Standards and Technology, 2013, URL: <https://qcrypt.github.io/2013.qcrypt.net/contributions/Shalm-slides.pdf>.
- [11] C. Autebert et al., *Direct measurement of the recovery time of superconducting nanowire single-photon detectors*, *Journal of applied physics* **128** (2020), URL: <https://doi.org/10.1063/5.0007976>.

Bibliography

- [12] S. Miki, M. Yabuno, T. Yamashita and H. Terai, *Stable, high-performance operation of a fiber-coupled superconducting nanowire avalanche photon detector*, *Optics express* **25** (2017) 6796, URL: <https://doi.org/10.1364/oe.25.006796>.
- [13] *Thorlabs - Your Source for Fiber Optics, Laser Diodes, Optical Instrumentation and Polarization Measurement Control*. URL: https://www.thorlabs.com/newgroupage9.cfm?objectgroup_id=3328%20Thorlabs%20-%20Powermeter%20specs.
- [14] *ND Filters: Mounted, AR Coated for 650 - 1050 nm*, URL: https://www.thorlabs.com/newgroupage9.cfm?objectgroup_id=6274.